

Catalytic Resonance Theory: Negative Dynamic Surfaces for Programmable Catalysts

Sallye R. Gathmann¹, M. Alexander Ardagh¹, Paul J. Dauenhauer^{1,*}

¹ Department of Chemical Engineering and Materials Science, University of Minnesota, 421 Washington Ave. SE, Minneapolis, MN 55455, USA

*Corresponding author: hauer@umn.edu

Abstract. Catalysts that change with time via programmed variation of their electronic occupation to accelerate surface reactions were evaluated in the case of negative adsorption energy scaling relations. Defined as the relative change in adsorption enthalpy, the gamma linear scaling parameter is negative when two adsorbates alternatively weaken and strengthen as catalysts are electronically perturbed. Simulations were conducted of a single transition state connecting two generic adsorbates representative of multiple reaction classes to understand the resulting negative gamma catalytic ratchet mechanism and its ability to accelerate catalytic reactions above the Sabatier peak and away from equilibrium. Relative to conventional positive gamma catalytic ratchets, the Sabatier volcanoes of negative gamma catalysis are narrower with greater enhancement of dynamic turnover frequency when catalysts are electronically oscillated. Promotion of the catalytic surface reaction forwards or backwards was predictable by a descriptor accounting for the relative rates of forward and reverse kinetics under oscillatory conditions.

1.0 Introduction. The emergence of cost-competitive solar and wind power in the past decade has transformed the landscape for renewable energy economics and applications.^[1,2] Produced in rural locations frequently far from industrial and urban centers, the challenge remains to store renewable energy for on-demand use across daily and seasonal requirements.^[3] Batteries, compressed air, and pumped water storage are potentially viable options for local electrical storage, but they remain stationary preferably near the location of energy generation.^[4,5] Alternatively, conversion of renewable electrical power to chemical energy in the form of liquid fuels such as ammonia or methanol provides the unique benefits of transportability and economic tradability as a commodity.^[6,7] Decoupling of energy generation, trading, and consumption via chemical energy liquids enables scenarios leading to offsetting of baseload power provided by conventional fossil-fuel-derived power and high rates of renewable energy implementation.^[8]

As depicted in **Figure 1a**, renewable energy such as wind and solar power can be captured and stored through distributed small-scale liquid fuel production via the conversion of available nitrogen (N₂, from air), water (H₂O), or carbon dioxide (CO₂,

from air). Water electrolyzed to hydrogen gas (H₂) can catalytically reduce N₂ or CO₂ to energy-dense liquid products ammonia (NH₃) or methanol (CH₃OH).^[9,10] The chemical processes to manufacture these liquids already exist at large scale via highly efficient, high-pressure catalytic processes, but scaling down these processes to match distributed energy generation is hindered by the unfavorable economics of small scale chemical processing.^[11] While novel process technologies such as small-scale separation via absorption have been developed to aid distributed liquid fuel manufacturing, the major limitations of such processes derive from poor catalyst performance and thermodynamic limitations.^[12,13]

For both catalytic chemistries (methanol and ammonia synthesis), conversion to the liquid product proceeds via sequential addition of hydrogen atoms as shown in **Figure 1b**. The optimal metal catalyst surface has been selected to bind adsorbates with sufficient strength to activate the core molecule (e.g., N₂ activation), promote hydrogenation, and permit desorption at a viable rate. However, catalysts must balance the kinetics of these different elementary steps and are thus limited to the Sabatier maximum catalytic rate.^[14,15,16] For ammonia synthesis, the high

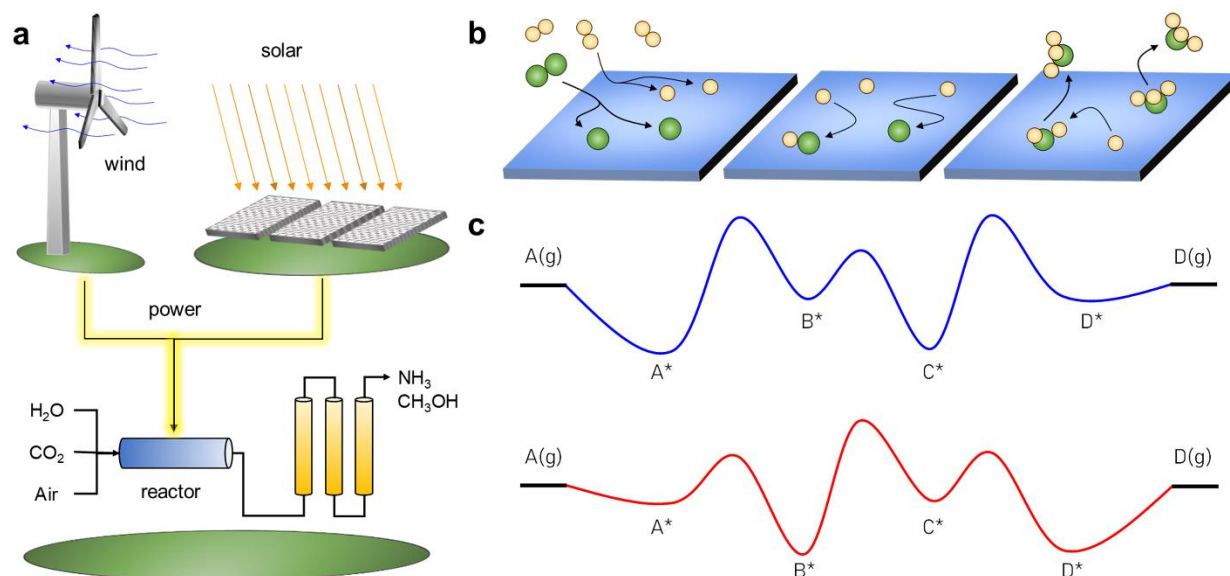


Figure 1. A renewable energy storage system based on negative catalytic dynamics. **(a)** Wind and solar energy drive a dynamic catalytic reactor within a co-located micro-process to manufacture fuels such as ammonia or methanol from air, water, or carbon dioxide. **(b)** Catalytic conversion of energy liquids requires multi-step hydrogenation for both ammonia and methanol synthesis. **(c)** Negative surface dynamics occur when surface binding energies of sequential surface intermediates change in opposite directions, thereby pushing adsorbates along a reaction sequence via a ratchet mechanism. In this case, the A-to-B-to-C-to-D reaction occurs with $\gamma_{B/A}$, $\gamma_{C/B}$, and $\gamma_{D/C}$ of -1.

activation barrier of the N₂ triple bond requires the catalytic reactor to operate at high temperature (~400 °C) for viable catalytic rates; at these conditions, ammonia production only becomes thermodynamically (and industrially) viable at high pressures (>150 atm) thereby raising the capital cost of equipment and operating costs associated with gas compression.^[17]

Enhancing catalytic rates above the Sabatier maximum for these energy-related chemistries requires a new approach to catalysis, such as forced catalyst dynamics (i.e., programmable catalysts). As previously shown via simulation^[18,19] and demonstrated by experiment with both dynamic photocatalysis^[20] and dynamic electrocatalysis,^[21] oscillating the binding energy of adsorbates on a catalytic surface accelerates the time-averaged turnover frequency orders of magnitude above the static maximum rate. This dynamic catalyst response depends on the selected applied oscillation frequency and amplitude, with a band of frequencies resonant with the underlying reaction kinetics yielding the highest catalytic rates. Through careful selection of the method of perturbation (e.g., light, electrical potential), catalytic material, and reaction conditions, optimal

dynamic promotion of the reaction can efficiently achieve one catalytic turnover per site per perturbing cycle of the catalytic surface.^[22]

While catalytic rate enhancement allows for lower reactor temperatures, a more significant opportunity for control of surface chemistry via programmable catalysts derives from the ratchet-like energy profile mechanism of the dynamic catalytic surface. Variation of the surface electronic state of the catalyst uniquely affects the binding state of different adsorbates, with some surface species shifting significantly more in binding energy than others. As previously shown,^[23] this asymmetry in surface binding yields a dynamic ratchet energy profile which biases the direction of the catalytic reaction; depending on the specific conditions, the added energy from modulating surface binding can drive reactions forward or backward away from equilibrium. While not yet found in reacting systems like synthetic heterogeneous catalysis, this dynamic energy phenomenon exists already in *unreactive* biological systems such as cell wall protein pumps, which utilize ATP for energy to drive Ca²⁺ and K⁺ ions into and out of cells away from their equilibrium distribution.^[24,25,26]

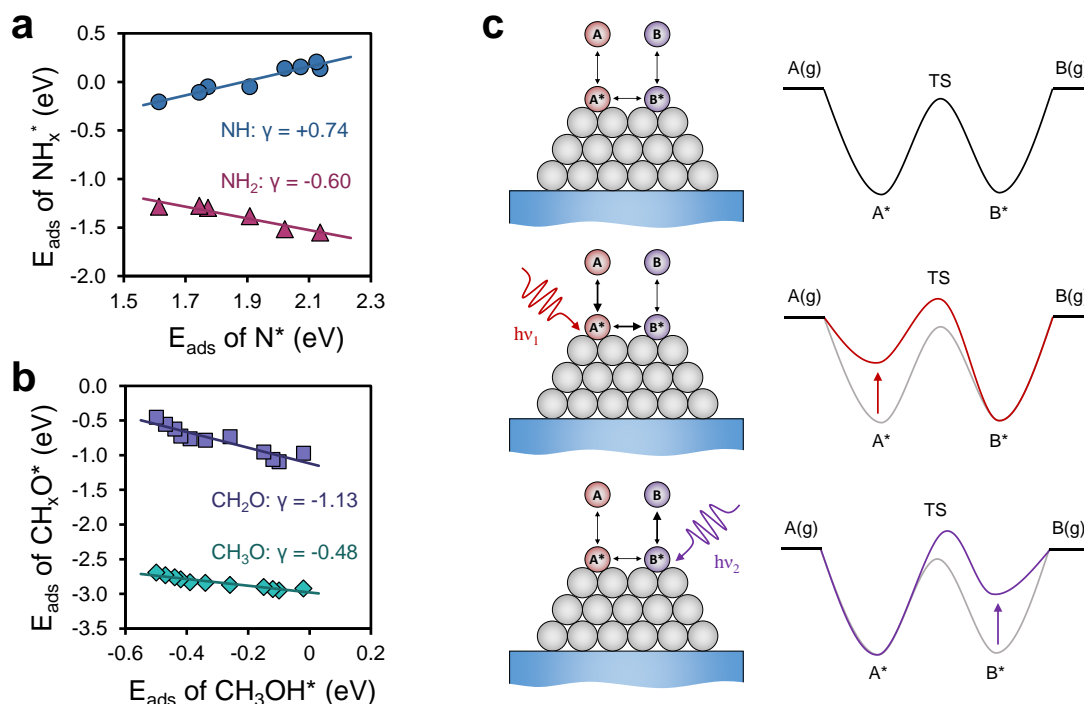


Figure 2. Negative gamma relationships of oxygen- and nitrogen-containing adsorbates. **(a)** N^* vs. NH_x^* on a molybdenum phosphide (MoP) catalyst demonstrates both positive and negative gamma relationships derived from P-site stability (i.e., hybridization of the binding site). **(b)** CH_3OH vs. CH_xO on a Ni(111) catalyst under $\pm 1.0 \text{ V/\AA}$ external electric field. **(c)** Effective negative gamma relationships also derive from selective manipulation of surface adsorbates such as photoexcitation by oscillation between two wavelengths that specifically reduce binding energy of A^* and B^* .

Adapting the surface ratchet energy mechanism to heterogeneous catalysis for energy applications can potentially improve system efficiency by controlling the extent of reaction. Conventional catalytic engineering methodologies select the reactor conditions (e.g., T , P_i , X_i) to achieve a favorable reaction equilibrium; catalysts are then adapted to accelerate rates in those conditions. Alternatively, a dynamic ratchet mechanism could operate at conditions with unfavorable reaction thermodynamics, with the reaction driven forward to a steady state away from equilibrium using the energy introduced through surface perturbation. For the example of ammonia synthesis, the goal is to reduce the pressure and temperature of the reactor and costs associated with gas compression. This reduces fluid phase thermodynamic selectivity to ammonia, thus requiring the reaction be driven to high yield of ammonia using surface work input via programmable catalysts.

In this work, the catalytic mechanism for driving unfavorable reactions to high conversion

and faster rates is evaluated via simulation of a model A-to-B reaction with a ratchet-like surface energy profile in which the binding energies of the two adsorbates shift in opposite directions. While we simulate a single surface reaction, one can imagine several of these catalytic ratchets linked together in series reactions to shuttle molecules along a more complex reaction pathway. As depicted in **Figure 1c**, the binding strength of surface adsorbates (A^* , B^* , C^* , and D^*) move in opposite directions as the surface energy profile shifts between two states (blue and red). For example, B^* binds strongly and A^* binds weakly in the red state, while A^* binds strongly and B^* binds weakly in the blue state. The ratio of change of the binding energies between the two states is referred to as ‘gamma’ ($\gamma_{\text{B/A}}$ defined as $\Delta\Delta H_{\text{B}}/\Delta\Delta H_{\text{A}}$) and is negative for the type of dynamic energy profile depicted in **Figure 1c**. These ratchet energy profiles serve to preferentially direct molecules along the reaction coordinate in the direction of the lower activation barrier, with the specifics of the

programmable catalyst determining if these lower barriers are along the forward or reverse reaction pathway. Identification of the key kinetic criteria leading to efficient catalytic pumping will serve as the foundation to translating this mechanism to key chemical energy storage technologies such as ammonia synthesis.

2.0 Results and Discussion. Programmable catalysis is a proposed design strategy capable of accelerating catalytic reaction rates above the Sabatier limit for a given reaction^[18] and selectively pushing reactions away from equilibrium via work input directly to the catalytic surface.^[23] The properties of inorganic catalysts are typically invariant with time (with the exceptions of restructuring and deactivation); therefore, implementation of dynamic catalysis requires the use of an external stimulus (e.g., strain, electric field) to drive desirable, periodic changes in the properties of a catalyst, such as its electronic occupation (i.e., d-band center). Numerous methods have been proposed for stimulating the catalytic surface to create desirable changes to surface-adsorbate interactions and, by extension, the reaction energy landscape and associated kinetic barriers.^[22] Each stimulus method elicits a unique change in the adsorbate-catalyst interaction, creating a wide parameter space that acts as an additional design option for optimization of dynamic reactions.

Changes to adsorption enthalpy result from changes in the electronic or steric properties of the catalyst due to new materials designs (i.e., alloys,^[27,28] site isolation,^[29,30] strained overlayers,^[31,32,33] etc.) or variation of the catalytic material altogether. The changes in adsorption energies of two reactive species relative to one another are described via linear scaling relationships,^[34] in which the adsorption enthalpy of the two molecules are plotted against one another as the material descriptor (e.g., d-band center) is altered. In general, positively correlated linear scaling relationships exist between molecules that bind through the same central atom, e.g., adsorption energies of ammonia synthesis intermediates (NH_x^*) scale linearly with the adsorption energy of the dissociated reactant (N^*) across transition metals.^[34,35] However, there are exceptions to this rule; negatively correlated scaling relationships have also been predicted for the same reaction

chemistry on a different type of catalytic material. Chan and co-workers^[36] calculated the adsorption energies of NH_x^* species on doped MoP surfaces using the P-site stability as the scaling descriptor. As depicted in **Figure 2a**, this leads to two distinct scaling relationships: NH^* scales positively with N^* (linear best fit slope $\gamma_{\text{NH}^*/\text{N}^*} = 0.74$), while NH_2^* scales negatively ($\gamma_{\text{NH}_2^*/\text{N}^*} = -0.60$), demonstrating that both ‘types’ (i.e., positively and negatively correlated) of scaling relationships can naturally co-exist using the same descriptor.

Negatively correlated scaling relationships ($\gamma < 0$) can also exist under applied external stimulus with unique periodic and perturbation scaling parameters. For example, catalytic synthesis of ammonia on ruthenium undergoing $\pm 4\%$ dynamic crystal strain has been predicted by Vlachos and coworkers to exhibit negative gamma dynamics for the N^* hydrogenation step when accounting for lateral interactions between adsorbed species, which can significantly change adsorption energies ($\gamma_{\text{NH}+\text{H}/\text{N}+2\text{H}} = -1.8$).^[37] They simulated the dynamic performance of this system, observing a 10-fold rate increase at an applied waveform frequency of 2 kHz for this complex chemical mechanism. In another example, negative scaling relationships have been predicted to exist for the methane steam reforming reaction, which is responsible for the majority of greenhouse gas emissions from the Haber-Bosch process.^[38] **Figure 2b** depicts two such scaling relationships for methane steam reforming intermediates on a Ni(111) catalyst under an applied $\pm 1.0 \text{ V/\AA}$ electric field calculated by McEwen and coworkers:^[39] CH_2O^* ($\gamma_{\text{CH}_2\text{O}^*/\text{CH}_3\text{OH}^*} = -1.13$) and CH_3O^* ($\gamma_{\text{CH}_3\text{O}^*/\text{CH}_3\text{OH}^*} = -0.48$) both negatively correlate with the adsorption energy of the methanol product, CH_3OH^* .

Another potential programmable catalysis implementation strategy combines two or more catalyst surface perturbations to achieve a synthetic negative gamma surface adsorption behavior. As depicted in **Figure 2c**, application of specific frequencies of light can selectively manipulate the adsorption energy of targeted surface intermediates. Application of one frequency (red, middle panel) selectively weakens the binding strength of the adsorbed reactant, while application of a second frequency (purple, bottom panel) now weakens that of the adsorbed product. Because the

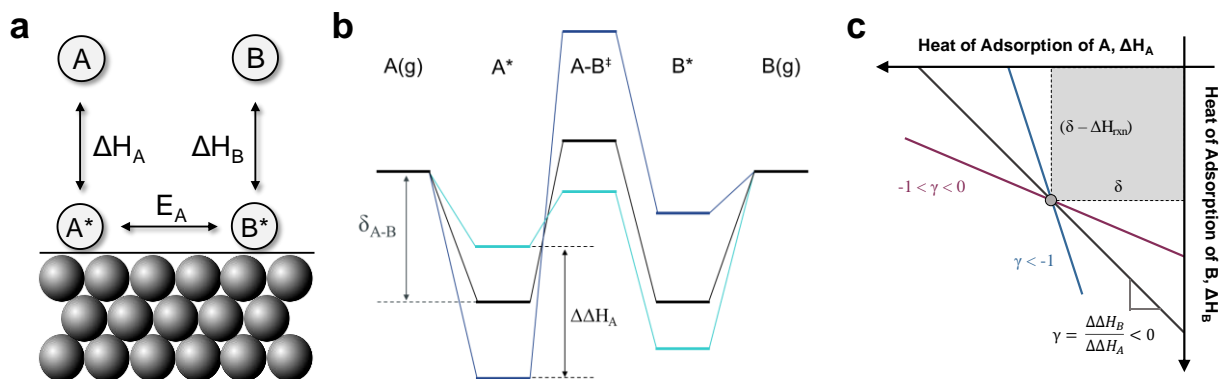
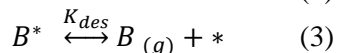
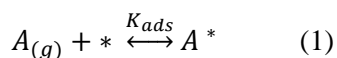


Figure 3. Computational modeling of negative gamma catalytic dynamics. **(a)** The catalytic conversion of A-to-B proceeds through surface species A* and B*. **(b)** Oscillation of the binding energy of component A* oppositely oscillates the binding energy of B* for negative gamma catalytic systems. **(c)** A gamma-delta plot of negative gamma catalytic systems.

applied light only perturbs the binding strength of one species at a time, the overall result is a ratcheting energy profile equivalent to a chemistry with $\gamma_{B/A} < 0$. Selective perturbation of metal-adsorbate bonds via targeted phonon frequencies has been demonstrated by Christopher and co-workers,^[22,20] application of light (425 nm) selectively weakened carbon monoxide (CO) binding energy on platinum nanoparticles (1 wt% Pt/Al₂O₃) without affecting nitric oxide (NO) binding energy.^[22,20] Optimizing this type of oscillating system will require a deeper understanding of the general dynamic behavior of negative gamma catalytic surfaces.

In this work, we investigated the performance of dynamic catalysis applied to an A-to-B model catalytic reaction in which the binding energies of A and B are linked through a negatively correlated linear scaling relationship described by proportionality parameter gamma, $\gamma < 0$. While this reaction is simpler than the multi-step series and/or parallel reaction sequences found in industrially relevant chemistries, the addition of dynamic surfaces to even a simple one-step reaction can exhibit complex and computationally demanding catalytic behavior.^[22] Moreover, the selection of a simple model reaction allowed us to map out catalytic performance across a wide parameter space associated with dynamic surfaces (e.g., varied frequency, amplitude). This provided general guidelines to inform materials design for either more detailed modeling of specific reactions or experimental implementation of dynamic catalytic systems.

2.1 Microkinetic Model. The A-to-B model catalytic reaction depicted in **Figure 3a** is comprised of three reversible elementary steps: (1) adsorption from the gas phase onto an active site of the catalytic surface, (2) unimolecular surface reaction, and (3) desorption to form the gaseous product.



Here, * represents an empty site, A* and B* are the surface-bound reaction intermediates, and K_i is the equilibrium constant for each reversible step.

The general reaction enthalpy diagram for a thermoneutral reaction ($\Delta G_{rxn} = 0$ kJ mol⁻¹) is shown in **Figure 3b**. The binding energies of A and B change due to forced catalyst surface perturbation; this change in catalyst state is represented by the two differently colored reaction energy profiles, with the change in the enthalpy of adsorption of the reactant defining the amplitude ($\Delta U_A = |\Delta\Delta H_A|$) of the imposed waveform. A ratchet-like profile is evident upon inspection of the enthalpy diagram: in the weak-binding state (sea green), the adsorbed reactant, A*, readily traverses over the low reaction barrier to react to B*, which is then trapped on the surface in an energetic well. Upon switching to the strong binding state (blue), the desorption barrier to B is lowered, while the

activation barrier of the reverse reaction prevents facile transformation back to the adsorbed reactant.

In our microkinetic model, we have selected the binding energy of A* ($BE_A = -\Delta H_A$) as the descriptor of the catalyst state, thus decoupling the identities of potential stimulating methods and catalytic materials from our general model. The relative response of the adsorbed product B* to the applied stimulus is modeled using the linear scaling relationships depicted in the gamma-delta plot of **Figure 3c**. Here, γ represents the linear slope (proportionality parameter) between the stimulus-driven changes in adsorption enthalpies of A* and B*,^[23]

$$\gamma = \Delta\Delta H_B / \Delta\Delta H_A = \Delta BE_B / \Delta BE_A \quad (4)$$

A second parameter, δ , defines the catalytic state (again, controlled by the applied stimulus) at which both surface species (A* and B*) have equivalent surface enthalpy,^[23]

$$\delta = H_A^*|_\delta = H_B^*|_\delta \quad (5)$$

This state is shown as the black reaction profile in **Figure 3b** and can be used as a boundary condition to derive a general expression for BE_B starting from equation 4,^[23]

$$BE_B = \gamma BE_A + \delta(1 - \gamma) + [H_B - \gamma H_A] \quad (6)$$

The above expression for BE_B can be simplified by removing the last two terms contained inside the square brackets for the thermoneutral reactions investigated in this work.

One additional relationship is required to fully specify the reaction coordinate by defining the transition state energy, or activation enthalpy of the forward reaction, at each catalytic state. The Brønsted-Evans-Polanyi relationship assumes a linear correlation between the heat of surface reaction ($\Delta H_{rxn} = H_B^* - H_A^*$) and activation enthalpy,^[40]

$$E_A = \alpha \Delta H_{rxn} + \beta \quad (7)$$

where α is the proportionality constant and β the constant offset parameter.

Rate equations for each elementary step were written according to the law of mass action, with

forward rate constants calculated using transition state theory and reverse rate constants from the respective equilibrium constant in order to ensure thermodynamic consistency.^[41] Altogether, the microkinetic model for an ideal (i.e., perfectly mixed), isothermal continuous stirred tank reactor (CSTR) was comprised of four differential equations, with examples for a gas-phase and surface-bound intermediate shown below, respectively,

$$r_j = \frac{d[j]}{dt} = v_{ij} \cdot r_i \left(\frac{N_{sites}}{V} \right) + \frac{\dot{q}}{V} ([j]_{feed} - [j]) \quad (8)$$

$$r_{\theta_j} = \frac{d\theta_j}{dt} = v_{ij} \cdot r_i \quad (9)$$

where \dot{q} is the reactor flowrate, V the reactor volume, and N_{sites} the number of catalytic sites in the CSTR reactor. Finally, a site balance (equation 10) completes the model by providing an algebraic constraint,

$$\theta^* + \theta_A^* + \theta_B^* = 1 \quad (10)$$

The catalytic reactor model is then specified through selection of six chemistry parameters (α , β , γ , δ , ΔH_{gas} , ΔS_{gas}), four reactor parameters (T , P , X_A , N_{sites}), and four dynamic parameters (frequency f , amplitude ΔU_A , oscillation endpoint or center point, and surface waveform shape such as square wave).

2.2 Static Catalyst Performance. Initial simulations evaluated the static catalytic performance (i.e., no surface binding oscillations) of the model reaction by varying the system descriptor, BE_A , as shown in **Figure 4**. The Sabatier volcano plots depicted in **Figure 4a** were simulated for gamma (γ) values ranging from -0.2 to -4.5. Fractional γ values, in which BE_A changes more than BE_B , are depicted in shades of pink, while the blue-shaded volcanoes depict γ values where the change in BE_B is of greater relative magnitude ($\gamma < -1$). The performance metric for these systems is the turnover frequency of product, B ($TOF_B [=] s^{-1}$), defined as follows for a reactor feed of pure reactant,

$$TOF_B = \frac{\dot{q}}{N_{sites}} [B_{(g)}] \quad (11)$$

Both the volcano width and peak TOF_B are a function of γ , with the smallest magnitude γ values

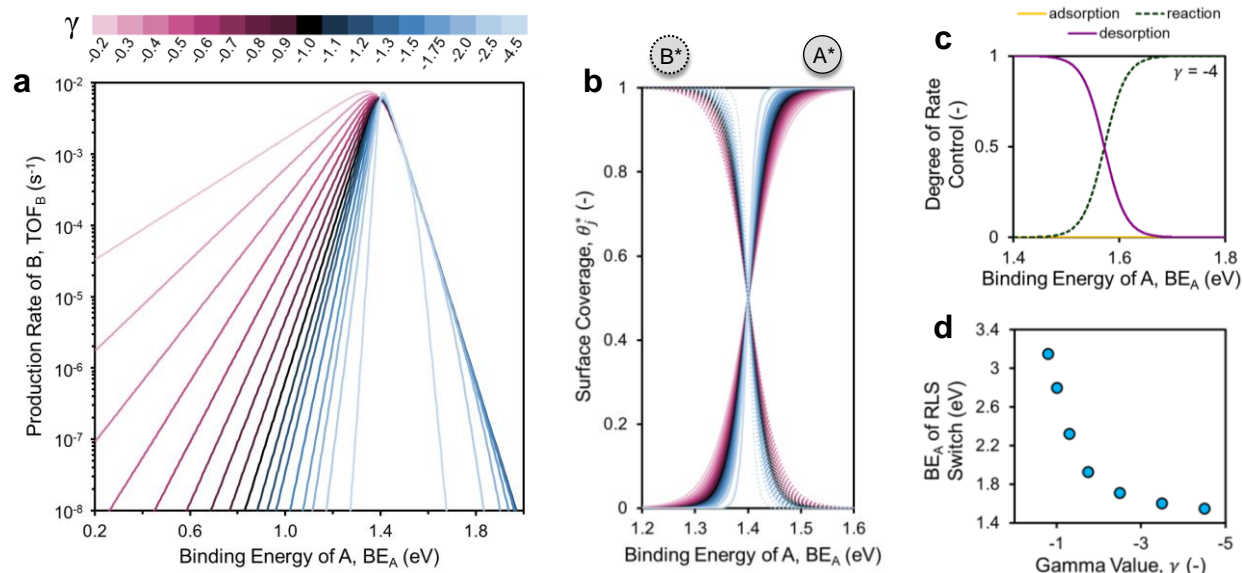


Figure 4. Supervolcano of negative gamma catalytic surfaces at static conditions. **(a)** Superimposed Sabatier volcanoes for gammas ranging from -0.2 to -4.5 show the accessible range of static turnover frequencies in a CSTR operating at differential conversion. **(b)** Surface coverage of A^* and B^* as a function of gamma and binding energy of A. The dominant surface species switches at δ (1.4 eV), where the surface enthalpies of both species are equal. **(c)** Example degree of rate control analysis for γ of -4, showing desorption is controlling at low BE_A and reaction is controlling at high BE_A . **(d)** Position on the volcano plot (BE_A) at which the rate limiting step (RLS) switches from desorption to reaction. Linear scaling parameters: $\alpha = 0.6$, $\beta = 102$ kJ/mol, $\delta = 1.4$ eV; reaction parameters: $\Delta H_{\text{ov}} = 0$ kJ/mol, $T = 200$ °C, 100 bar A feed pressure, 1% conversion of B.

producing the widest volcanoes due to the lower sensitivity of BE_B to perturbations in BE_A as γ approaches zero. The optimal static performance, or Sabatier volcano peak, varied from a TOF_B of 5.9 to 7.4 ms^{-1} for γ of -1.0 and -4.5, respectively. In general, the extreme values of γ yielded slightly higher turnover frequencies, while γ of -1, where the binding energies of A and B changed in exactly equal and opposite directions, was the lowest. All volcano peaks were within 0.06 eV of the point of equivalent surface enthalpy, δ (1.4 eV).

Figure 4b depicts surface coverage changes as a function of BE_A near the delta point, which was the only region of appreciable surface coverage change across the supervolcano. At low values of BE_A relative to δ ($\text{BE}_A < 1.2$ eV), the surface was fully saturated with B^* , while at high binding energy of A^* ($\text{BE}_A > 1.6$ eV) the surface was instead saturated with A^* . The surface coverages of the adsorbed product and reactant are equal at the delta point, consistent with its definition as the point of equivalent surface enthalpy between the two surface species, A^* and B^* , in a moderate-temperature reactor. The γ value determined the width of the surface coverage transition region,

with the fractional gamma values ($-1 < \gamma < 0$) again resulting in wider transition regions. Notably, there is no range of BE_A values where the surface is largely vacant; with the inverse proportionality parameter ($\gamma < 0$), one surface species will always be strong binding. This is different from the positive gamma ($\gamma > 0$) catalytic systems, where binding energies of both surface adsorbates (A^* and B^*) weaken or strengthen simultaneously, leading to an abundance of empty active catalyst sites for overall weak binding conditions.^[23]

The shape of the Sabatier volcano for each reaction is determined by the rate-limiting elementary step (RDS) for each value of the system descriptor, in this case BE_A . Therefore, the surface coverage and kinetic behavior of these catalytic systems can be rationalized from inspection of the reaction coordinate diagrams (**Figure 3b**), which indicate which elementary step will be rate limiting on either slope of the volcano. For example, at low BE_A (see green reaction profile) where B^* is the most thermodynamically stable surface species, both the forward and reverse kinetic barriers (i.e., desorption and reverse reaction, respectively) for B^* are far higher than those for A^* . This is

consistent with high surface coverage of B* in this region of the volcano ($0.2 < BE_A < 1.4$ eV) and suggests that desorption will be the RDS for $BE_A < \delta$. Similarly, when BE_A is strong (blue reaction profile), an analysis of the reaction coordinate supports the observed high coverage of A* and suggests that surface reaction will be the RDS.

Upon inspection of the supervolcano (**Figure 4a**), it is evident that this simple analysis is not perfectly consistent with the microkinetic model output: in a kinetic regime with a sole RDS and near-unity surface coverage of one species, the slope of the volcano will be a function of γ . For example, at low BE_A where the surface coverage of B* is ~ 1 , the rate of formation of B is approximately equal to the forward rate constant of desorption, k_{des,B^*} . Recalling that the forward rate constants are calculated using transition state theory and thus depend on reaction thermodynamics, the volcano slope should reflect this dependence on the value of γ . The volcano slope can be extrapolated from its desorption-limited rate expression to obtain the following expression, which is a function of γ , as expected,

$$\left. \frac{\partial \log TOF_B}{\partial BE_A} \right|_{low BE_A} = \frac{\partial \log r_B}{\partial BE_A} = -\frac{\gamma}{2.3 RT} \quad (12)$$

A similar derivation of the volcano slope at high BE_A assuming a surface reaction limited kinetic regime and near-unity surface coverage of A* also yields a γ -dependent volcano slope:

$$\left. \frac{\partial \log TOF_B}{\partial BE_A} \right|_{high BE_A} = -\frac{\alpha(1-\gamma)}{2.3 RT} \quad (13)$$

Here, the Brønsted-Evans-Polanyi proportionality parameter is also included in the expression, because the forward rate constant of reaction, $k_{f,rxn}$, is a function of the activation energy. Full derivations of equations 12 and 13 are included in the SI (section S1).

As can be seen from the above expressions for the volcano slopes, each individual volcano plot within the supervolcano envelope ($-0.2 < \gamma < -4.5$ eV) should have its own distinct slopes in any kinetic regime with a single rate-determining step (RDS) and near-unity coverage of one species; the second condition is always satisfied for BE_A values outside of the surface coverage transition region

depicted in **Figure 4b**. This behavior is apparent in the low- BE_A side of the supervolcano ($BE_A < 1.2$ eV), where each individual volcano has a different slope. In contrast, the high- BE_A ($BE_A > 1.6$ eV) slopes all fall onto the same curve for the majority of the γ values simulated, suggesting that this half of the volcano is not solely reaction-limited as predicted from inspection of the reaction coordinate diagrams.

To quantitatively determine the rate-determining step (RDS) of each volcano plot, a degree of rate control (DRC) analysis was conducted for a subset of γ values (details, SI section S2). A DRC value of unity indicates that a step is the sole RDS, while a DRC value of zero indicates negligible control over the net catalytic rate; intermediate values are calculated when multiple elementary steps influence the overall rate.^[42] **Figure 4c** shows an example DRC output for γ of -4. For $BE_A < 1.5$ eV, desorption of B* (purple) is the sole rate-determining step; above 1.7 eV, the sole RDS switches to the surface reaction of A* to B* (green, dashed). As expected from the surface coverage data, there is no BE_A range where adsorption of A(g) exerts any control over the reaction rate. The DRC analysis is summarized in **Figure 4d** over a range of γ values, wherein the value of BE_A at which the RDS switches from desorption of B* to surface reaction (i.e., the crossover point ~ 1.6 eV depicted in **Figure 4c**) is plotted. As γ becomes more negative, the BE_A at which this switch occurs decreases in value asymptotically approaching the delta point, δ of 1.4 eV.

Put together, this A-to-B model catalytic reaction with negative gamma ($\gamma < 0$) forms kinetic volcanoes of static catalysts with two distinct transitions visible in **Figure 4a**. The transition at the peak derives from the change in the most abundant surface intermediate at the point of equivalent surface enthalpy, δ . Since the region near the volcano peak is controlled almost entirely by the rate of B* desorption, the overall production rate of B(g) decreases at BE_A values above the peak where the surface coverage of B* rapidly decreases. The second transition occurs at higher values of BE_A , where individual volcanoes with γ less than negative one ($\gamma < -1$) separate from an asymptote that represents a decreasing overall catalytic rate resulting from lower surface coverage of B*. This second transition occurs only for highly negative

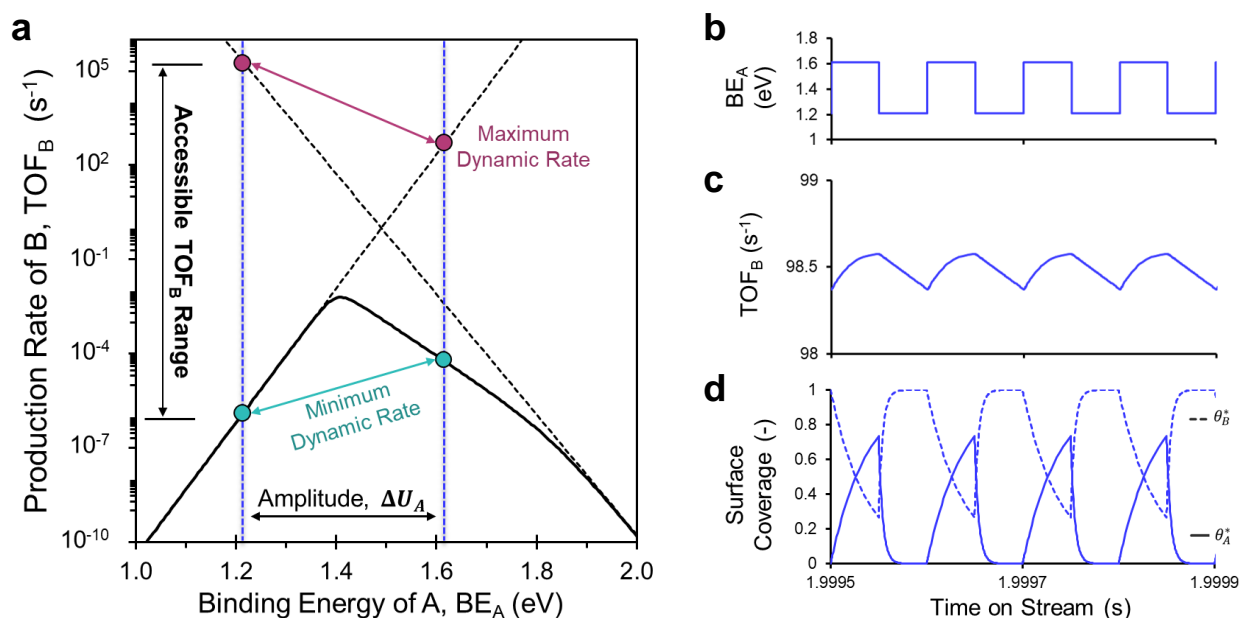


Figure 5. Dynamic CSTR operating at differential conversion under an applied square waveform. **(a)** Volcano plot showing the accessible turnover frequency range for the static system. **(b)** Model input, binding energy of A (BE_A), and model outputs **(c)** turnover frequency of B (TOF_B) and **(d)** surface coverages of A* and B* (θ_A and θ_B) changing with time due to forced oscillations in the catalyst properties, which drives changes in BE_A . Linear scaling parameters: $\alpha = 0.6$, $\beta = 102$ kJ/mol, $\gamma = -2.0$, $\delta = 1.4$ eV; reaction parameters: $\Delta H_{ov} = 0$ kJ/mol, $T = 200$ °C, 100 bar A feed pressure, 1% time-averaged conversion of B; waveform parameters: 50% duty cycle square waveform centered at the volcano peak (1.41 eV) with amplitude $\Delta U_A = 0.4$ eV and frequency $f = 10^4$ Hz.

gamma systems where the rate determining step shifts from desorption of B* to the surface catalytic reaction.

2.3 Dynamic Rate Enhancement.

Implementing dynamic catalysis on surfaces with negative gamma linear scaling between reactant and product oscillates the binding energy of A* (BE_A) between opposite sides of the Sabatier volcano peak where the reaction is controlled by different rate-determining elementary steps and most abundant surface species. **Figure 5a** depicts the Sabatier volcano for γ of -2 with a volcano peak centered (BE_A of 1.41 eV) waveform with fixed oscillation amplitude, ΔU_A , of 0.4 eV. The oscillation endpoints are indicated by two vertical dashed blue lines at BE_A of 1.21 and 1.61 eV. As demonstrated in previous work,^[22] the performance of this waveform depends on its frequency; modulating this dynamic parameter allows for almost eight decades of variation in the TOF_B range (approx. $\sim 10^{-5}$ s $^{-1}$ to $\sim 10^3$ s $^{-1}$), which includes catalytic rates that outperform the static volcano peak (TOF_B of 6.3 ms $^{-1}$). At low applied oscillation frequencies ($< \sim 10^{-3}$ Hz), the reaction system

behaves as if it is a combination of the two static states at each waveform endpoint, thus achieving a dynamic TOF_B that is represented by the sea green tie line below the volcano peak (simulated time-averaged TOF_B of 3.4×10^{-5} s $^{-1}$; see Figure S5-1). When the frequency is increased to $\sim 10^5$ Hz or higher, it becomes resonant with the underlying elementary step frequencies; this frequency can be identified by the pink tie line with endpoints at the intersection of the surface oscillation amplitude endpoints (vertical blue dashed lines) and the black dashed lines that extend from the sides of the Sabatier volcano. The lower- TOF_B of these two intersection points is the maximum accessible turnover frequency ($TOF_B \sim 10^3$ s $^{-1}$).

To simulate dynamic catalysis, the binding energy of A* was varied as a square waveform as depicted in **Figure 5b**. This waveform shape was selected based on prior simulations that showed square waveforms to be the most efficient waveform shape (as compared to sinusoidal, sawtooth, or triangular), because the catalyst exists only at the extremes of the descriptor value (i.e., BE_A) during oscillation.^[18] Surface chemical

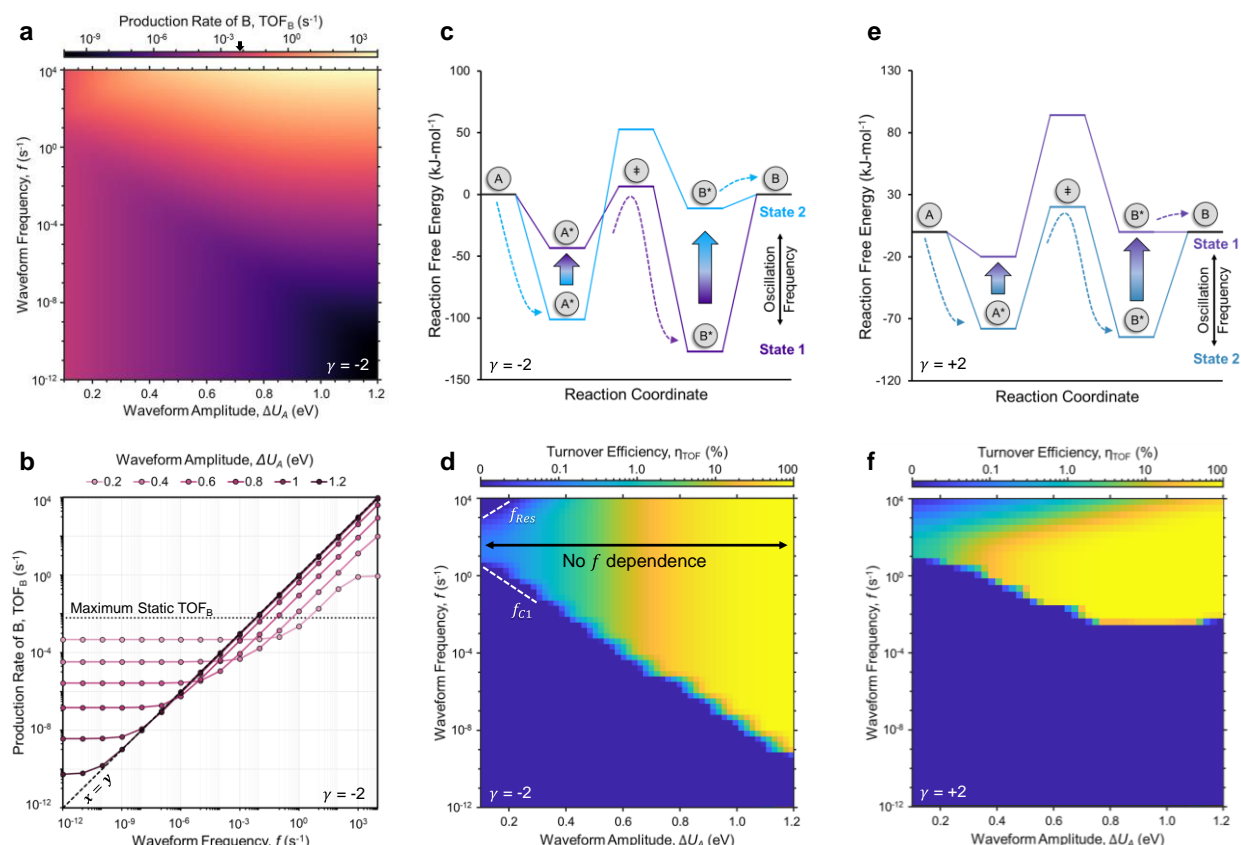


Figure 6. Performance of a negative gamma (γ of -2) dynamic catalyst operating with a CSTR operating at differential conversion under an applied catalyst square waveform with variable amplitude and frequency. **(a)** Time-averaged turnover frequency of B (TOF_B, color) across variations in catalyst waveform amplitude and frequency. Maximum static TOF_B indicated by black arrow on color bar legend. **(b)** Frequency response of select oscillation amplitudes ($0.2 \leq \Delta U_A \leq 1.2$). Dashed parity line represents the maximum theoretical performance. **(c)** Reaction coordinate diagram (ΔU_A of 0.6 eV) showing the kinetically decoupled elementary steps: surface reaction is promoted during state 1 (purple), while desorption is promoted during state 2 (blue). **(d)** Turnover efficiency (η_{TOF} , color) for varying catalyst waveform amplitudes and frequencies. **(e)** Reaction coordinate diagram for γ of +2 with ΔU_A of 0.6 eV amplitude showing the mechanism of dynamic rate enhancement for positive gamma systems. **(f)** Turnover efficiency (η_{TOF} , color) for γ of +2 with varied catalyst waveform amplitude and frequencies. Linear scaling parameters: $\alpha = 0.6$, $\beta = 102$ kJ/mol, $\gamma = -2.0$, $\delta = 1.4$ eV; reaction parameters: $\Delta H_{ov} = 0$ kJ/mol, $T = 200$ °C, 100 bar A feed pressure, 1% time-averaged conversion of B; waveform parameters: square waveform centered at the volcano peak (1.41 eV and 1.17 eV for γ of -2 and +2, respectively) operating at 50% duty cycle.

response to the forced catalyst dynamics at frequency f of 10^4 Hz is shown in **Figure 5c-d**. Both the TOF_B and surface coverage oscillate due to the periodic variation in BE_A , with higher instantaneous catalytic rates observed at the stronger BE_A oscillation endpoint. The dynamic time-averaged TOF_B of 98.5 s⁻¹ (an average of the oscillation in **Figure 5c**) was lower than the maximum dynamic rate predicted by the pink tie line in **Figure 5a** due to an insufficiently high applied oscillation frequency; higher applied frequencies would achieve higher TOF_B because the applied waveform frequency is below the

resonance frequency. The dynamic surface behavior is depicted in **Figure 5d**, where the surface alternates between high coverages of either A* or B* as BE_A alternates between strong and weak binding, respectively. The time-averaged coverages of A* and B* are 0.25 and 0.75, respectively, and the coverage of empty sites is negligible as expected.

Broader evaluation of applied catalyst dynamic parameters for the γ of -2 system depicted in **Figure 5** was conducted by varying both the waveform amplitude ($0.1 \leq \Delta U_A \leq 1.2$ eV) and frequency ($10^{-12} \leq f \leq 10^4$ Hz); results are summarized in

Figure 6. The heat map of **Figure 6a** depicts variation of the dynamic TOF_B (color: black to purple to yellow) as a function of amplitude and frequency. The darker colors in the lower right region of the plot represent undesirable catalyst waveform amplitude-frequency combinations that yield the lowest dynamic TOF_B ; alternatively, the lightest shaded region in the upper right indicates the fastest combinations of amplitude and frequency that outperform the volcano peak by multiple orders of magnitude. Both performance extremes occur at the largest amplitude (ΔU_A of 1.2 eV), while smaller amplitudes exhibit a lower range of dynamic TOF_B . For example, the TOF_B ranges by just over one order of magnitude for ΔU_A of 0.1 eV, while the catalytic rate varies over six orders of magnitude for ΔU_A of 0.4 eV. Significantly, all sampled amplitudes can achieve catalytic rates above the Sabatier volcano peak (marked with black arrow on color scale) and exhibit around one to over five orders of magnitude rate enhancement at $f \geq 1.0$ Hz, which is a readily achievable oscillation frequency for many possible catalyst perturbation methods.^[22]

The catalytic frequency response to applied catalyst surface oscillations with variable amplitude is depicted in **Figure 6b**. Considering the frequency response curve of ΔU_A of 0.2 eV, three distinct kinetic regions are observed as the frequency is increased. At $f \leq 0.1$ Hz, the catalytic turnover frequency is constant at a $\text{TOF}_B \sim 0.46 \text{ ms}^{-1}$ due to the slow waveform oscillation which allows each amplitude endpoint to achieve steady-state. At these low waveform oscillation frequencies, the entire catalytic system acts as a combination of the two static endpoints as predicted by the green tie line in **Figure 5a**. For applied catalyst frequencies between 0.1 and 1,000 Hz, the catalyst responds to the applied stimulus by increasing TOF_B in accordance with the increased catalyst waveform frequency. Finally, applied frequencies above 1,000 Hz are in resonance with the underlying reaction kinetics of this particular set of waveform parameters, yielding a resonant TOF_B of 0.89 s^{-1} . This resonant catalytic rate represents the highest dynamic performance of the $\Delta U_A = 0.2 \text{ eV}$ square waveform, which is about two orders of magnitude greater than the static maximum rate of 6.3 ms^{-1} at the Sabatier volcano peak. As the applied catalyst waveform increases in amplitude ($\Delta U_A > 0.2 \text{ eV}$), the intermediate region exhibiting increasing TOF_B

exists over a broader range of applied oscillation frequencies. Notably, larger amplitude waveforms did not enter a resonance band within the sampled range of applied catalyst frequencies, leading to simulated TOF_B values up to 10^4 s^{-1} (dynamic rate enhancement of over 100,000 \times the volcano peak). While other physical limitations such as diffusion (not included in our microkinetic model) will limit turnover frequencies this fast, these $\gamma < 0$ catalytic systems show immense potential for rate enhancement at experimentally feasible oscillation amplitudes ($\Delta U_A \sim 0.4 \text{ eV}$).^[22]

The mechanism of dynamic rate enhancement is illustrated in **Figure 6c**, which shows the reaction energy profile of a 0.6 eV amplitude (ΔU_A) waveform centered at the volcano peak for γ of -2. State 1 (purple) is the reaction energy profile of the weak-binding A^* , while state 2 (blue) is strong-binding A^* . At state 1, A^* proceeds over the lowered forward reaction barrier to produce B^* , which accumulates on the surface due its strong adsorption energy. Upon switching to state 2 (blue), the desorption barrier for B^* is lowered and B^* readily desorbs from the surface to form the gas-phase product, $B(g)$. This empties surface sites, which are quickly filled by $A(g)$ adsorbing to form A^* and thus the catalytic cycle is completed. The simulated periodic cycling of surface coverages shown in **Figure 5d** are in agreement with this proposed rate enhancement mechanism.

A second consideration when optimizing programmable catalysts is their turnover efficiency. Defined previously,^[22] this metric quantifies the number of forced oscillation cycles required per catalytic turnover; a system operating at 100% efficiency will achieve one catalytic turnover to produce $B(g)$ from $A(g)$ per imposed oscillation cycle. Catalytic turnover efficiency is defined as,

$$\eta_{\text{TOF}} = \frac{(\text{dynamic TOF}_B) - (\text{average static TOF}_B)}{f} \cdot 100\% \quad (14)$$

where f is the applied surface oscillation frequency, and the average static TOF_B is calculated according to the waveform endpoints and duty cycle. For example, recalling the green minimum rate tie line in **Figure 5a** whose endpoints exist on the volcano curve itself, the average static TOF_B of $3.4 \times 10^{-5} \text{ s}^{-1}$ is simply the arithmetic mean of the tie line

endpoints for the 50% duty cycle waveforms used throughout this study.

The turnover efficiency (η_{TOF}) of the dynamic catalytic reaction system with γ of -2 is summarized in the heat map of **Figure 6d** for variable applied oscillation amplitude ($0.1 \leq \Delta U_A \leq 1.2$ eV) and frequency ($10^{-12} \leq f \leq 10^4$ Hz). The dark blue area ($\eta_{TOF} = 0\%$) at the lower left corner represents a region of negligible dynamic response; surface binding energy oscillations provide no rate enhancement at these low waveform frequencies, consistent with the horizontal, low-frequency region of the reaction rate response curves in **Figure 6b**. However, once the catalytic reaction rate begins to increase with increasing forced oscillation of BE_A at the first corner frequency (f_{C1} in **Figure 6d**), η_{TOF} also increases. For a fixed applied oscillation amplitude, the region of positive η_{TOF} extends to frequencies up to the start of the resonance band of frequencies (f_{res} in **Figure 6d**), above which η_{TOF} rapidly decreases back to zero. Low η_{TOF} in the resonance band is due to a fixed catalytic rate at resonance conditions; as described in equation 14, increases in applied dynamic catalyst frequency, f , with a constant numerator decreases η_{TOF} . Most significantly, the turnover frequency of these dynamic systems can be maximized without decreasing turnover efficiency by operating right at the lowest frequency of the resonance range.

A beneficial feature of negative dynamic catalytic systems visible in **Figure 6d** is their constant catalytic turnover efficiency at fixed ΔU_A in the range of frequencies between the first corner frequency and resonance band (see Figure S6-2a for an alternate depiction). Moreover, the η_{TOF} increases substantially in this region with increasing amplitude, ranging from <1% at amplitudes $\Delta U_A < 0.4$ eV up to over 90% efficiency at $\Delta U_A \geq 1.1$ eV. This indicates that negative γ dynamic catalytic reactions can operate at high efficiency even at low rates of reaction, provided the amplitude of the imposed surface oscillation is sufficiently large. For example, a catalytic reaction with applied frequency, f , of 10^{-6} Hz and amplitude, ΔU_A , of 0.8 eV has a η_{TOF} of 41%; increasing ΔU_A to 1.0 eV doubles η_{TOF} to 83%.

For comparison, positive ($\gamma > 0$) dynamic systems were also investigated. **Figure 6e** depicts the reaction energy profile of a γ of +2 system that

is comparable with the γ of -2 system depicted in **Figure 6c**, i.e., a 0.6 eV amplitude waveform centered at the respective volcano peak; the mechanism of dynamic rate enhancement elucidated in earlier work^[23] is also illustrated. **Figure 6f** depicts this system's η_{TOF} as a function of amplitude and frequency. Comparing to **Figure 6d**, the high- η_{TOF} region extends to lower amplitudes (ΔU_A of 0.4 eV). However, this positive- γ system does not exhibit a range of frequency-independent η_{TOF} other than at large amplitudes (see also Figure S6-2b); this is due to the lower resonance frequencies of the γ of +2 system (Figure S6-3), which means that the η_{TOF} decreases at the simulated upper waveform frequency range. Thus, $\gamma < 0$ systems can achieve higher rate enhancement without decreasing their turnover efficiency in comparison to their $\gamma > 0$ counterparts.

An additional handle available for optimizing dynamic systems is the oscillation position along the descriptor scale of the binding energy of A^* (BE_A), which in a real catalytic device could be controlled by selecting the starting catalytic material (e.g., metal element). While the simulations of **Figures 5** and **6** fixed the catalyst surface oscillation amplitude center point to the volcano peak, another option is to utilize constant oscillation amplitude with different waveform center points, effectively moving the waveform along the BE_A descriptor scale across the volcano plot. As depicted in **Figure 7a**, a surface oscillation ΔU_A of 0.2 eV has a waveform center point that can either be located directly above a Sabatier peak of a particular catalytic system or on either side, leading to variable dynamic catalytic performance. These amplitude positions were compared between two systems with a γ of +2 and -2 using the metric of dynamic rate enhancement (DRE) with the following definition,

$$DRE = \frac{\text{Dynamic rate}}{\text{Sabatier peak rate}} \quad (15)$$

By this definition, the DRE metric quantifies the rate increase beyond the maximum rate of the static catalyst, which exists at the Sabatier peak. As shown in **Figure 7a**, the dynamic catalytic system with γ of -2 system achieves DRE of 180, which significantly exceeds that of γ of +2 (DRE of only ~10). The maximum dynamic catalytic rate of both

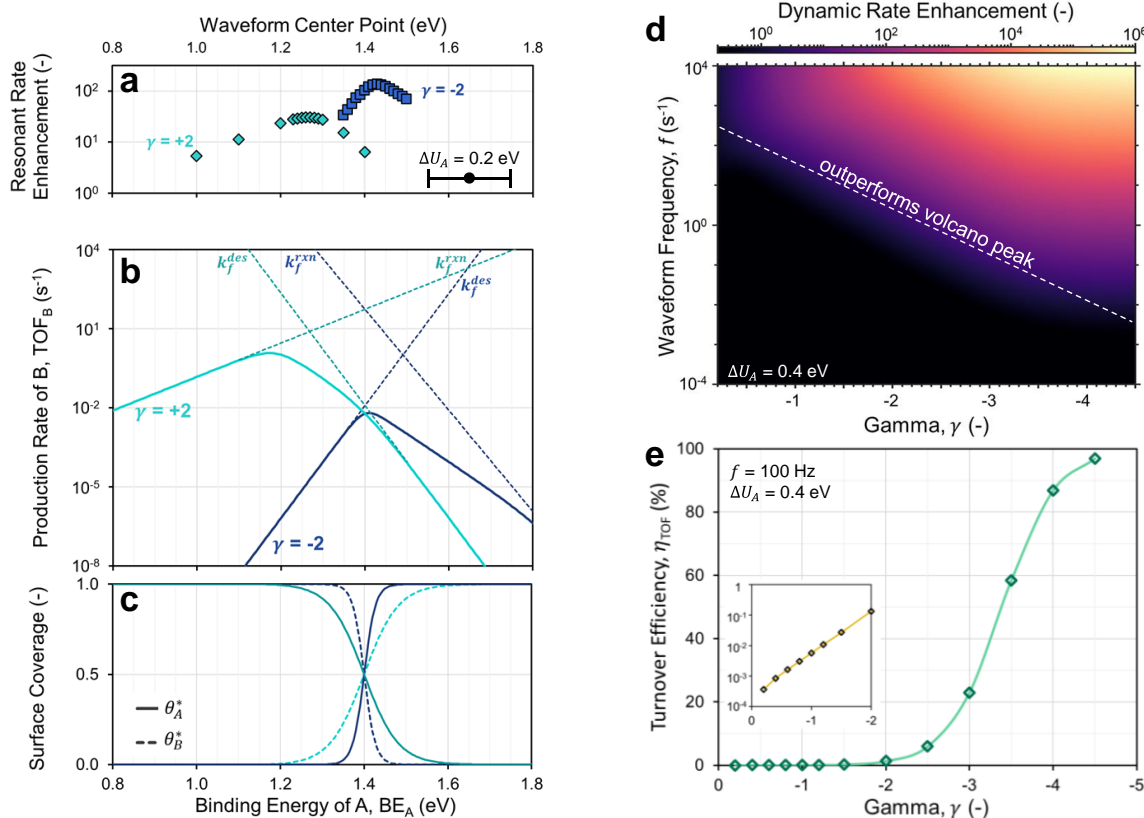


Figure 7. Impact of dynamic parameters on the dynamic performance of a CSTR operating at differential conversion under an applied square waveform. (a) Dynamic rate enhancement at resonance as a function of 0.2 eV amplitude waveform center point. (b) Volcano plots and (c) surface coverage plots as a function of BE_A showing static system performance for comparison. (d) Dynamic rate enhancement (color) as a function of γ and waveform frequency for 0.4 eV waveform amplitude. (e) Turnover efficiency as a function of γ at 100 Hz applied waveform frequency. Inset shows efficiency for fractional gammas in logarithmic scale. Linear scaling parameters: $\alpha = 0.6$, $\beta = 102$ kJ/mol, $\delta = 1.4$ eV; reaction parameters: $\Delta H_{ov} = 0$ kJ/mol, $T = 200^\circ\text{C}$, 100 bar A feed pressure, 1% time-averaged conversion of B; waveform parameters: square waveform operating at 50% duty cycle (a-c) variable center point or (d-e) centered at each respective volcano peak.

systems occurred for oscillation amplitudes centered at BE_A values slightly higher than the volcano peak. The maximum rate of the γ of +2 dynamic catalytic system occurs at BE_A of 1.27 eV, while the maximum rate of the γ of -2 dynamic catalytic system occurs at BE_A of 1.43 eV. The location of the maximum dynamic rate enhancement differs from both the Sabatier or 'inverted' volcano peaks (dashed lines in **Figure 7b**) and the δ point (1.4 eV), at which the surface coverage changes between A* and B* (**Figure 7c**; dynamic coverages in Figure S6-5); it also does not align with the RDS transition point calculated for either value of γ (Figure S6-6). Thus, simulations are required to predict the precise optimal waveform center point.

Next, the impact of the proportionality parameter γ on rate enhancement was investigated using ΔU_A of 0.4 eV waveforms centered at each respective volcano peak. **Figure 7d** depicts the results of this study in a heatmap of dynamic rate enhancement, DRE, (color: black to purple to yellow) as a function of γ and frequency. Black shaded regions indicate waveform frequencies at which the system underperforms the respective volcano peak (DRE < 1), while increasingly lighter colors indicate higher performance at which the dynamic resonant TOF_B is above the Sabatier peak. At f of 10⁴ Hz, DRE ranges from about one order of magnitude above the volcano peak for γ of -0.2, up to over 10⁶ times faster than the rate at the peak for γ of -4.5. DRE above unity is observed over a wider

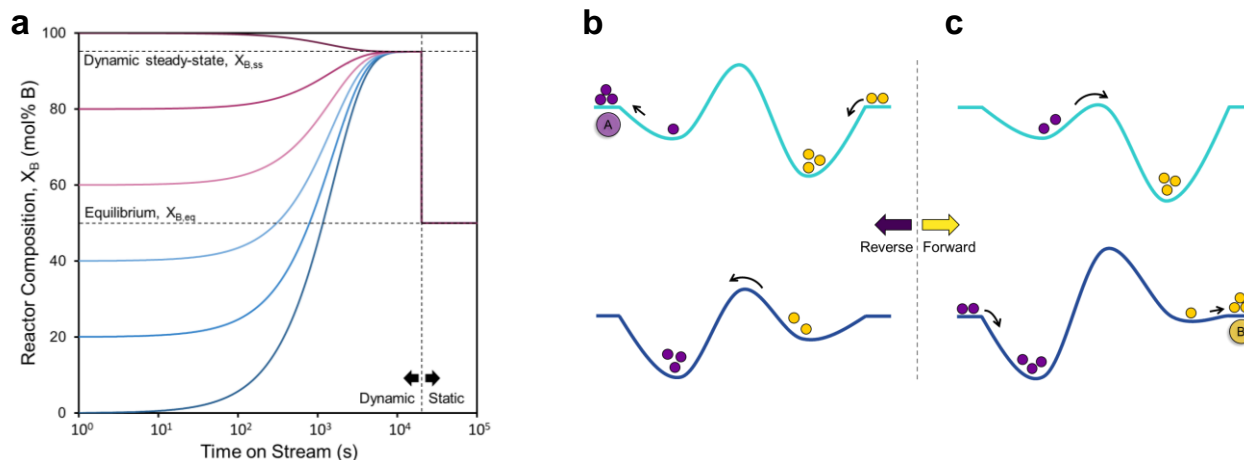


Figure 8. Batch reactor with dynamic catalyst promoting A(g) to B(g) reaction. **(a)** Batch reactor composition (mol% B) as a function of time on stream for a delta-centered waveform with amplitude $\Delta U_A = 0.6$ eV and frequency f of 1.0 Hz. All initial feed conditions achieve the same dynamic steady-state (93 mol% B), and when the dynamic surface modulation is stopped, the reactor composition immediately returns to the equilibrium composition of 50%. LSR parameters: $\alpha = 0.6$, $\beta = 102$ kJ/mol, $\gamma = -2$, $\delta = 1.4$ eV; reaction parameters: $\Delta H_{ov} = 0$ kJ/mol, $T = 300^\circ\text{C}$, varied A feed pressure; waveform parameters: square waveform operating at 50% duty cycle centered at the delta point. **(b)** Illustrative reaction energy profile of a system that promotes the reverse reaction under dynamic operation showing molecules shuttled backwards along the reaction pathway during surface oscillation. **(c)** Illustration of the mechanism by which a dynamic system promotes the forward reaction to B.

frequency band for larger magnitude values of γ . For example, the DRE frequency band is ~ 1 decade of frequency modulation wide for γ of -0.2, compared to > 6 decades for the largest magnitude γ simulated of -4.5. These results are consistent with expectations that larger magnitude gammas will provide faster catalytic kinetics under dynamic stimulation due to the ability to elicit larger favorable changes to the reaction energy landscape for the same change in BE_A ; they also show that these larger magnitude gamma catalytic systems outperform the Sabatier peak ($DRE > 1$) across wider ranges of the dynamic parameters.

Finally, the γ -dependence of turnover efficiency was studied by fixing the waveform amplitude at ΔU_A of 0.4 eV and allowing the γ value to vary from -0.2 to -4.5 as shown in **Figure 7e**, which features a sigmoidal relationship between η_{TOF} and γ . To eliminate dependence on frequency, η_{TOF} values were compared at applied oscillation frequency, f , of 100 Hz, which is within the ‘frequency plateau’ of all sampled gamma values (Figure S6-8). For $\gamma \geq -2$, the efficiency values are poor (see inset; $\eta_{TOF} < 1\%$); however, as γ becomes more negative the efficiencies increase up to $\sim 97\%$ for γ of -4.5; higher efficiencies are likely obtainable at even more negative γ values. In the

earlier varied-amplitude study for γ of -2 (**Figure 6**), low efficiencies observed at smaller values of ΔU_A were due to either failure of the surface coverage to turn over during an applied oscillation cycle (Figure S6-1) and/or significant rates of reverse surface reaction due to the comparable barrier heights of desorption and reverse surface reaction. The latter cause of inefficiency explains the η_{TOF} trends as a function of γ in **Figure 7e** and can be rationalized by comparing the respective multistate reaction energy profiles at fixed ΔU_A of 0.4 eV (Figure S6-10): for small-magnitude γ values, the binding energy of BE_B is similar at both oscillation endpoints (energy states), while for large negative γ values, a small perturbation in BE_A results in large changes in BE_B . In turn, these changes in BE_B result in favorable changes to the kinetic barriers of the forward reaction which are larger in magnitude for large negative γ values, thus leading to a more efficient ‘ratchet’ mechanism of promoting the forward reaction.

2.4 Negative Gamma Dynamic Steady-State.

One method for driving reactions away from equilibrium is adding work directly through the catalytic surface via dynamic catalysis.^[23] **Figure 8a** depicts the reactor composition (X_B) changes with time under dynamic operation of a catalyst

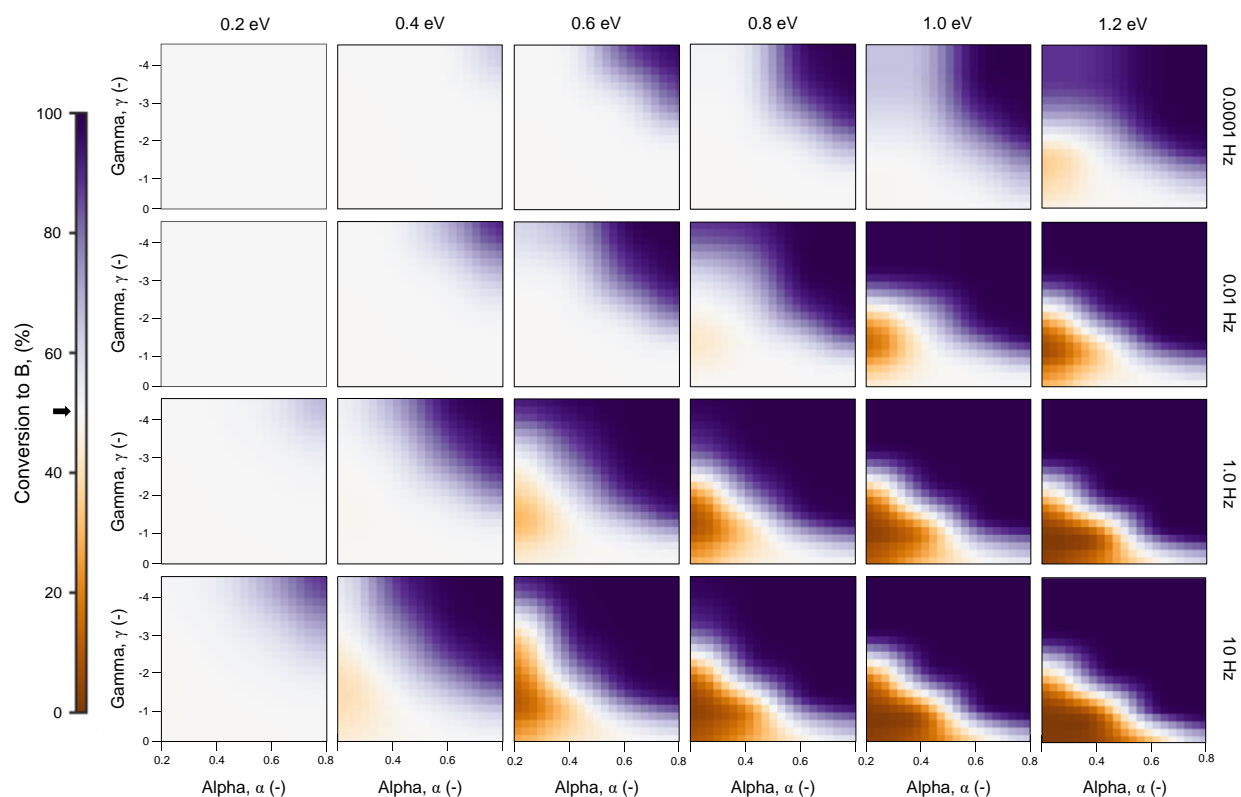


Figure 9. Multiparameter study to determine outcomes of batch reactor steady-state conversion as a function of reaction chemistry and catalyst-stimulus pairing. Parameters α , γ , ΔU_A and f were varied throughout simulations, while β and δ were held constant at 100 kJ·mol⁻¹ and 1.4 eV, respectively. Simulations were carried out in a $\Delta H_{ov} = 0$ kJ·mol⁻¹ batch reactor at 300°C utilizing a square waveform centered at the delta point.

within a batch reactor with surface waveform amplitude ΔU_A of 0.6 eV and frequency f of 1.0 Hz. Under dynamic catalyst operation, reactor gas composition achieves a dynamic steady-state composition of ~93 mol% B, independent of the initial reactor gas composition. Upon returning to static operation where the binding energies of A* and B* are invariant with time, the reactor composition immediately returns to its equilibrium composition $X_{B,eq}$ of 50%, as dictated by the gas-phase reaction thermodynamics ($\Delta G_{gas} = 0$ kJ mol⁻¹). Thus, dynamic perturbation of the catalytic surface allows for reversible changes in chemical conversion.

While the simulation depicted in **Figure 8a** promotes the forward reaction to conversion greater than equilibrium conversion of 50%, it is possible for negative gamma dynamic catalysts to promote catalytic reactions either forward or backwards, depending on the selected parameters. **Figure 8b** illustrates the mechanism by which the reverse reaction is promoted, leading to $X_{B,ss} < X_{B,eq}$. In

these systems, the reverse reaction barriers are no longer prohibitively large, allowing B* to traverse the reverse surface reaction to A* and desorb to form A(g) as the overall reaction product. Conversely, **Figure 8c** depicts an example of a dynamic catalyst that promotes the forward reaction ($X_{B,ss} > X_{B,eq}$). Here, the reverse kinetic barriers are sufficiently large such that only the forward reaction proceeds at appreciable rates and the reactant is effectively shuttled forward along the reaction coordinate to form the favored product, B(g).

2.5 Asymmetric Catalytic Ratchet Directionality. To determine the relationship between dynamic catalytic parameters and the directionality of the negative gamma catalytic ratchet (forwards or backwards), batch reactor simulations were carried out using a delta-centered square waveform with varied values of gamma ($-4.5 \leq \gamma \leq -0.2$), alpha ($0.2 \leq \alpha \leq 0.8$), waveform amplitude ($0.2 \leq \Delta U_A \leq 1.2$ eV), and waveform frequency ($10^{-6} \leq f \leq 10$ Hz). The simulated

steady-state reactor composition ($X_{B,ss}$) for all permutations of dynamic catalyst parameters is shown in **Figure 9**, with white depicting gas-phase equilibrium and purple and orange indicating forward (more B) and backwards (more A) catalytic bias, respectively. By the distribution of color across the entire data set, there are two key observations: (1) more bias of the reaction away from equilibrium occurs at larger amplitude and higher applied frequencies, and (2) there exists two distinct regions of forward and backwards bias on a map of gamma ($0 < \gamma < 4.5$) versus alpha ($0.2 < \alpha < 0.8$) parameters. The reaction is pushed past equilibrium with higher conversion to B(g) for large alpha and gamma parameters, while the reverse reaction is promoted at low gamma and low alpha parameters. The dividing line between forward and reverse reaction, at which point the system operates at the static equilibrium conversion, is always a diagonal line; its exact position in the **Figure 9** heatmaps shifts based on the applied waveform parameters.

These observations are consistent with statistical analysis of the batch reactor dynamic steady state data. To identify key variables, covariance between the time-averaged, steady-state dynamic reactor composition in **Figure 9** ($X_{B,ss}$, mol% B) and each dynamic parameter was calculated using Pearson's correlation, a measure of the linear correlation between two variables (details, SI section S7-1).^[43] As shown in **Figure 10a**, the parameters α and γ have a significant correlation with the steady-state reactor composition, $X_{B,ss}$, with Pearson's correlation coefficients of 0.45 and -0.44, respectively. Accordingly, these two parameters have a substantial impact on the directionality of the reaction as shown in the heatmaps of **Figure 9**. Notably, the waveform amplitude, ΔU_A , and frequency, f , do not have significant correlation with $X_{B,ss}$ across the entire data set (correlation values < 0.2 were treated as insignificant in our analysis). These two parameters only have a substantial impact on $X_{B,ss}$ for a fixed reaction chemistry (i.e., fixed α and γ), where they control the extent to which the reaction moves away from equilibrium (Figure S7-1).

Predicting the directionality of negative gamma catalytic surfaces requires a relationship between programmable catalyst parameters and the resulting catalytic performance. We propose a directionality

descriptor, \mathcal{J} (pronounced “läm”), as the ratio of the forward and reverse time constants (equations 16 and 17, respectively) of the overall reaction. The time constants for the overall forward and reverse reaction directions are calculated as the reciprocal sum of the rate constants,

$$\tau_f = \frac{1}{k_{f,rxn}} + \frac{1}{k_{des,B^*}} \quad (16)$$

$$\tau_r = \frac{1}{k_{r,rxn}} + \frac{1}{k_{des,A^*}} \quad (17)$$

where $k_{f,rxn}$ and $k_{r,rxn}$ are the forward and reverse rate constants for surface reaction, respectively, and k_{des,j^*} is the desorption constant for species j . Due to the negative relationship between binding energies of A^* and B^* , the time-averaged surface coverages of these two species is almost always $\sim 50\%$ and therefore surface coverages are not considered in this directionality descriptor.

Because the reaction energy landscape changes with time due to the forced oscillation of BE_A , this time constant ratio (τ_f/τ_r) is calculated independently at each square waveform endpoint. The complete directionality descriptor is then defined as the product of these two ratios,

$$\mathcal{J} = \left(\frac{\tau_f}{\tau_r} \Big|_{low\ BE_A} \right) \left(\frac{\tau_f}{\tau_r} \Big|_{high\ BE_A} \right) \quad (18)$$

This descriptor can be simplified by considering only the kinetically relevant rate constants, where the faster rate constants drop out of the expression in equations 16 and 17 due to the reciprocal sums (details, SI section S7-2). This simplified descriptor becomes,

$$\mathcal{J} \sim \frac{k_{r,rxn}|_{low\ BE_A}}{k_{f,rxn}|_{high\ BE_A}} \cdot \frac{k_{des,A^*}|_{high\ BE_A}}{k_{des,B^*}|_{low\ BE_A}} \quad (19)$$

The effectiveness of the proposed descriptor, \mathcal{J} , is apparent when plotted against the $X_{B,ss}$ for over 1,400 data points as shown in **Figure 10b**. As expected from its definition, the regions of forward and backward reaction are divided by a \mathcal{J} value of unity. The upper right region highlighted with a yellow background, in which the forward reaction to B is promoted ($X_{B,ss} > 50\%$), correlates with \mathcal{J} greater than 1.0, while the light-blue shaded region, where the reverse reaction to A is promoted ($X_{B,ss} <$

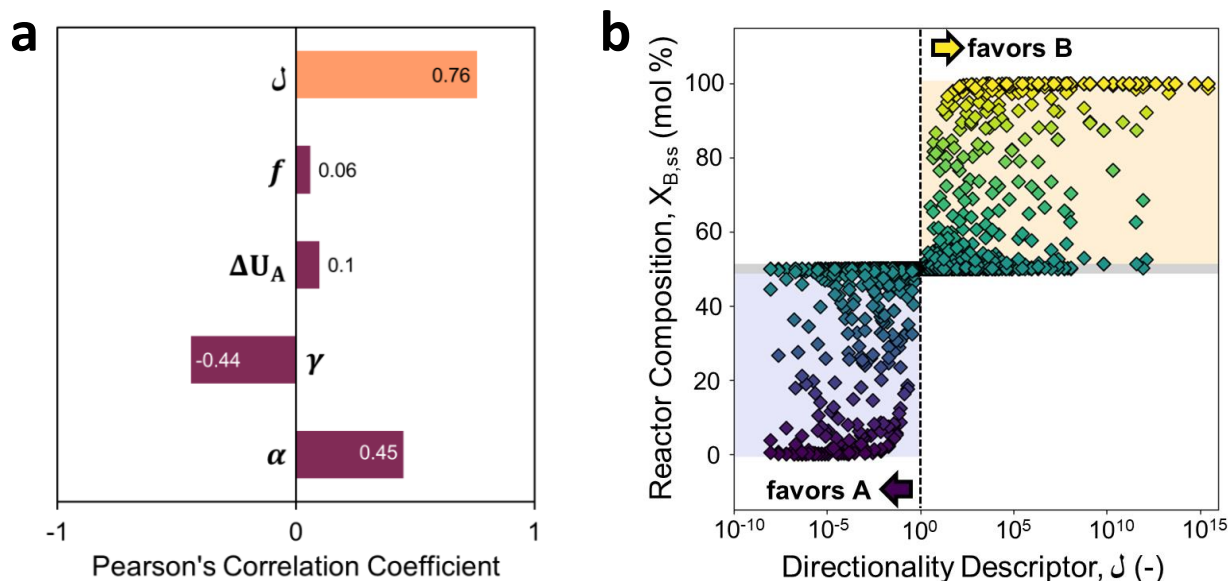


Figure 10. Directionality of a batch reactor with a negative gamma dynamic catalyst. (a) Covariance between various dynamic parameters and the steady-state reactor composition, $X_{B,ss}$, as determined by Pearson's correlation coefficient. The correlation between the derived descriptor, \Downarrow , and $X_{B,ss}$ is shown in the orange bar. (b) The derived directionality descriptor plotted against the simulation results. For \Downarrow values less than 1, the reverse reaction is promoted (purple shaded region), and for values greater than 1, the forward reaction is promoted (yellow shaded region). Grey horizontal bar, scaled to marker width, represents conditions at which the dynamic batch reactor returns the static equilibrium composition. Simulation parameters: variable α , γ , ΔU_A and f ; $\beta = 100$ kJ/mol, $\delta = 1.4$ eV, $\Delta H_{ov} = 0$ kJ/mol; batch reactor at $T = 300$ °C with 100 bar A(g) initial charge; delta-centered symmetric square waveform.

50%), correlates with \Downarrow less than 1.0. Any reaction that yields \Downarrow of 1.0 only achieves gas-phase equilibrium reactor composition (50% A(g), 50% B(g)), independent of the applied dynamic waveform conditions; this is the only case where we expect that adding work directly to a catalytic surface cannot perturb the catalytic reaction away gas-phase equilibrium. In our study, this was only observed for one parameter combination simulated: for γ of -1.5 and α of 0.4, the value of \Downarrow was always unity and the simulated $X_{B,ss}$ was always 50% at all waveform conditions used in this study. As demonstrated by the absence of outliers in **Figure 10b**, the directionality descriptor \Downarrow is robust in its ability to predict whether a reaction will proceed forwards or backwards based only on estimating the reaction rate constants utilizing transition state theory. However, \Downarrow cannot predict a priori the extent to which the reaction is moved away from equilibrium; full simulation is required to quantify $X_{B,ss}$ due to its dependence on waveform frequency, which is not captured in \Downarrow .

In summary, a programmable catalyst can be utilized to drive a reaction either forwards or backwards through careful selection of the catalytic

material and perturbation method. Notably, based on how the transition state is affected by the surface work input, reactions with a wide range of gamma values ($-3.0 \leq \gamma < -0.2$) can be driven in either the forwards or reverse direction. This is particularly promising for methanol and ammonia synthesis, where the $\gamma_{B/A}$ values reported (**Figure 2** and text discussion) are often > -1 , which was previously expected to only promote the reverse reaction.^[23] Nevertheless, additional studies are needed to understand how transition states scale with surface perturbation and to discover the optimal programmable catalyst materials and perturbation methods for the more complex chemistries of liquid fuel synthesis.

3.0 Conclusions. Catalytic surface chemistries exhibiting negative gamma linear scaling in surface reactant and surface product through a common transition state form a narrow Sabatier volcano with a maximum in catalytic turnover frequency. The Sabatier peak forms near the delta (δ) point, defined as the energy where both surface reactant and product have the same enthalpy of adsorption; at this condition, the surface coverage switches

between the two surface species to balance the rate of catalytic reaction and desorption. Oscillation of catalyst electronic state causes the surface reactant and product to vary in binding energy between each side of the Sabatier volcano and promotes the net catalytic reaction to rates that are orders of magnitude above the Sabatier peak, with higher applied frequencies and larger amplitudes of surface binding energy oscillation yielding the highest catalytic rates. Maximum catalytic rates are achieved at resonance frequencies, with the largest amplitude surface oscillations producing the widest band of resonant frequencies. Negative gamma dynamics also promote the catalytic surface reaction forward or backward away from equilibrium, achieving almost complete conversion in either direction depending on the chemistry and applied oscillation parameters. A descriptor comprised of the relative rate constants of forward and reverse reactions for all conditions of catalyst oscillation predicted the directionality of dynamic catalytic promotion.

4.0 Methods. The microkinetic model described in the results and discussion was simulated using Matlab 2019/2020a. The differential equations were solved using built-in solver ode15s with minimum solver tolerances of 10^{-6} relative and 10^{-8} absolute due to the ultra-stiff nature of the model. For the continuous stirred-tank reactor (CSTR) simulations, the reactor inlet flowrate (\dot{q}) was varied until 1% conversion of A(g) was achieved at steady-state; batch reactor simulations were allowed to run until steady-state was reached after charging the reactor with 100 bar A initial charge. Time-averaged concentration and coverage values during dynamic catalysis were calculated by numerical integration over 20 or more oscillation periods using Matlab's built-in 'trapz' function. Steady-state was defined as $\leq 10^{-4}$ [M] absolute difference in the time-averaged concentration of A(g) over these 20 oscillations. All CSTR simulations were carried out at a reactor temperature of 200°C; batch reactor simulation temperature was increased to 300°C to decrease computation time.

Heat maps depicting the simulation results were created by interpolating a grid of discrete data points obtained by varying oscillation amplitudes, frequencies, and gamma values. The 'linear' interpolation method was used after linearizing the

raw data points; after interpolation, all data was transformed out of the log space for displaying the heat map. Turnover efficiency (η_{TOF} , **Figure 6d-6f**) values at oscillation frequencies under the first corner frequency were set to zero to remove unphysical high-efficiency data points.

Acknowledgements. The authors acknowledge the Minnesota Supercomputing Institute (MSI) at the University of Minnesota for providing resources that contributed to the results reported within this paper. Sallye Gathmann was supported by the National Science Foundation Graduate Research Fellowship under Grant CON-75851, Project 00074041. We thank Professor Dan Frisbie and Professor Omar Abdelrahman for insightful discussions.

Keywords. Energy, Catalysis, Storage, Dynamics

Supporting Information. Additional details including the calculation of the turnover efficiency are available in the supporting information (Section S4); additional methods of data extrapolation (Section S3) and batch reactor covariance analysis (Section S7-1) are also included. Digital copies of the data tables are available at the Data Repository of the University of Minnesota (DRUM).

References

- (1) Cornwall, W. Renewable Power Surges as Pandemic Scrambles Global Energy Outlook, New Report Finds. *Science* **2020**.
<https://doi.org/10.1126/science.abc5463>.
- (2) Mitchell, C. Momentum Is Increasing towards a Flexible Electricity System Based on Renewables. *Nature Energy* **2016**, 1 (2).
<https://doi.org/10.1038/nenergy.2015.30>.
- (3) Arbabzadeh, M.; Sioshansi, R.; Johnson, J. X.; Keoleian, G. A. The Role of Energy Storage in Deep Decarbonization of Electricity Production. *Nature Communications* **2019**, 10 (1).
<https://doi.org/10.1038/s41467-019-11161-5>.
- (4) Bogdanov, D.; Farfan, J.; Sadovskaia, K.; Aghahosseini, A.; Child, M.; Gulagi, A.; Oyewo, A. S.; de Souza Noel Simas Barbosa, L.; Breyer, C. Radical Transformation Pathway towards Sustainable Electricity via Evolutionary Steps. *Nature Communications* **2019**, 10 (1).
<https://doi.org/10.1038/s41467-019-08855-1>.

- (5) Service, R. Giant Batteries and Cheap Solar Power Are Shoving Fossil Fuels off the Grid. *Science* **2019**. <https://doi.org/10.1126/science.aay7094>.
- (6) Service, R. Ammonia—a Renewable Fuel Made from Sun, Air, and Water—Could Power the Globe without Carbon. *Science* **2018**. <https://doi.org/10.1126/science.aau7489>.
- (7) Palys, M. J.; Daoutidis, P. Using Hydrogen and Ammonia for Renewable Energy Storage: A Geographically Comprehensive Techno-Economic Study. *Computers and Chemical Engineering* **2020**, *136*. <https://doi.org/10.1016/j.compchemeng.2020.106785>.
- (8) Davis, S. J.; Lewis, N. S.; Shaner, M.; Aggarwal, S.; Arent, D.; Azevedo, I. L.; Benson, S. M.; Bradley, T.; Brouwer, J.; Chiang, Y. M.; Clack, C. T. M.; Cohen, A.; Doig, S.; Edmonds, J.; Fennell, P.; Field, C. B.; Hannegan, B.; Hodge, B. M.; Hoffert, M. I.; Ingersoll, E.; Jaramillo, P.; Lackner, K. S.; Mach, K. J.; Mastrandrea, M.; Ogden, J.; Peterson, P. F.; Sanchez, D. L.; Sperling, D.; Stagner, J.; Trancik, J. E.; Yang, C. J.; Caldeira, K. Net-Zero Emissions Energy Systems. *Science* **2018**, *360* (6396). <https://doi.org/10.1126/science.aas9793>.
- (9) Glenk, G.; Reichelstein, S. Economics of Converting Renewable Power to Hydrogen. *Nature Energy* **2019**, *4* (3), 216–222. <https://doi.org/10.1038/s41560-019-0326-1>.
- (10) Ojha, D. K.; Kale, M. J.; Dauenhauer, P. J.; McCormick, A.; Cussler, E. L. Desorption in Ammonia Manufacture from Stranded Wind Energy. *ACS Sustainable Chemistry & Engineering* **2020**. <https://doi.org/10.1021/acssuschemeng.0c03154>.
- (11) Palys, M. J.; Allman, A.; Daoutidis, P. Exploring the Benefits of Modular Renewable-Powered Ammonia Production: A Supply Chain Optimization Study. *Industrial and Engineering Chemistry Research* **2019**, *58* (15), 5898–5908. <https://doi.org/10.1021/acs.iecr.8b04189>.
- (12) Guo, W.; Vlachos, D. G. Patched Bimetallic Surfaces Are Active Catalysts for Ammonia Decomposition. *Nature Communications* **2015**, *6*. <https://doi.org/10.1038/ncomms9619>.
- (13) Song, Y.; Johnson, D.; Peng, R.; Hensley, D. K.; Bonnesen, P. V.; Liang, L.; Huang, J.; Yang, F.; Zhang, F.; Qiao, R.; Baddorf, A. P.; Tschaplinski, T. J.; Engle, N. L.; Hatzell, M. C.; Wu, Z.; Cullen, D. A.; Meyer, H. M.; Sumpter, B. G.; Rondinone, A. J. A Physical Catalyst for the Electrolysis of Nitrogen to Ammonia. *Science Advances* **2018**, *4* (4). <https://doi.org/10.1126/sciadv.1700336>.
- (14) Logadottir, A.; Rod, T. H.; Nørskov, J. K.; Hammer, B.; Dahl, S.; Jacobsen, C. J. H. The Brønsted-Evans-Polanyi Relation and the Volcano Plot for Ammonia Synthesis over Transition Metal Catalysts. *Journal of Catalysis* **2001**, *197* (2), 229–231. <https://doi.org/10.1006/jcat.2000.3087>.
- (15) Hellman, A.; Baerends, E. J.; Biczysko, M.; Bligaard, T.; Christensen, C. H.; Clary, D. C.; Dahl, S.; Van Harreveld, R.; Honkala, K.; Jonsson, H.; Kroes, G. J.; Luppi, M.; Manthe, U.; Nørskov, J. K.; Olsen, R. A.; Rossmeisl, J.; Skúlason, E.; Tautermann, C. S.; Varandas, A. J. C.; Vincent, J. K. Predicting Catalysis: Understanding Ammonia Synthesis from First-Principles Calculations. *Journal of Physical Chemistry B* **2006**, *110* (36), 17719–17735. <https://doi.org/10.1021/jp056982h>.
- (16) Honkala, K.; Hellman, A.; Remediakis, I. N.; Logadottir, A.; Carlsson, A.; Dahl, S.; Christensen, C. H.; Nørskov, J. K. Ammonia Synthesis from First-Principles Calculations. *Science* **2005**, *307* (5709), 555–558. <https://doi.org/10.1126/science.1106435>.
- (17) Pattabathula, V.; Richardson, J. Introduction to Ammonia Production. *Chemical Engineering Progress* **2016**, No. 9, 69–75.
- (18) Ardagh, M. A.; Abdelrahman, O. A.; Dauenhauer, P. J. Principles of Dynamic Heterogeneous Catalysis: Surface Resonance and Turnover Frequency Response. *ACS Catalysis* **2019**, *9* (8), 6929–6937. <https://doi.org/10.1021/acscatal.9b01606>.
- (19) Ardagh, M. A.; Shetty, M.; Kuznetsov, A.; Zhang, Q.; Christopher, P.; Vlachos, D. G.; Abdelrahman, O. A.; Dauenhauer, P. J. Catalytic Resonance Theory: Parallel Reaction Pathway Control. *Chemical Science* **2020**, *11* (13), 3501–3510. <https://doi.org/10.1039/c9sc06140a>.
- (20) Qi, J.; Resasco, J.; Robotjazi, H.; Alvarez, I. B.; Abdelrahman, O.; Dauenhauer, P.; Christopher, P. Dynamic Control of Elementary Step Energetics via Pulsed Illumination Enhances Photocatalysis on Metal Nanoparticles. *ACS Energy Letters* **2020**, *5*, 3518–3525. <https://doi.org/10.1021/acsenenergylett.0c01978>.
- (21) Gopeesingh, J.; Ardagh, M. A.; Shetty, M.; Burke, S. T.; Dauenhauer, P. J.; Abdelrahman, O. A. Resonance-Promoted Formic Acid Oxidation via Dynamic Electrocatalytic Modulation. *ACS Catalysis* **2020**, *10* (17), 9932–9942. <https://doi.org/10.1021/acscatal.0c02201>.

- (22) Shetty, M.; Walton, A.; Gathmann, S. R.; Ardagh, M. A.; Gopeesingh, J.; Resasco, J.; Birol, T.; Zhang, Q.; Tsapatsis, M.; Vlachos, D. G.; Christopher, P.; Frisbie, C. D.; Abdelrahman, O. A.; Dauenhauer, P. J. The Catalytic Mechanics of Dynamic Surfaces: Stimulating Methods for Promoting Catalytic Resonance. *ACS Catalysis* **2020**, 12666–12695. <https://doi.org/10.1021/acscatal.0c03336>.
- (23) Ardagh, M. A.; Birol, T.; Zhang, Q.; Abdelrahman, O. A.; Dauenhauer, P. J. Catalytic Resonance Theory: SuperVolcanoes, Catalytic Molecular Pumps, and Oscillatory Steady State. *Catalysis Science and Technology* **2019**, 9 (18), 5058–5076. <https://doi.org/10.1039/c9cy01543d>.
- (24) Tsong, T. Y.; Xie, T. D. Ion Pump as Molecular Ratchet and Effects of Noise: Electric Activation of Cation Pumping by Na,K-ATPase. *Applied Physics A: Materials Science and Processing* **2002**, 75 (2), 345–352. <https://doi.org/10.1007/s003390201407>.
- (25) Astumian, R. D. Adiabatic Pumping Mechanism for Ion Motive ATPases. *Physical Review Letters* **2003**, 91 (11). <https://doi.org/10.1103/PhysRevLett.91.118102>.
- (26) Apell, H. J. Structure-Function Relationship in P-Type ATPases—a Biophysical Approach. *Reviews of physiology, biochemistry and pharmacology* **2003**, 150, 1–35. <https://doi.org/10.1007/s10254-003-0018-9>.
- (27) Hannagan, R. T.; Giannakakis, G.; Flytzani-Stephanopoulos, M.; Sykes, E. C. H. Single-Atom Alloy Catalysis. *Chemical Reviews* **2020**, 120 (21), 12044–12088. <https://doi.org/10.1021/acs.chemrev.0c00078>.
- (28) Greiner, M. T.; Jones, T. E.; Beeg, S.; Zwiener, L.; Scherzer, M.; Girgsdies, F.; Piccinin, S.; Armbrüster, M.; Knop-Gericke, A.; Schlögl, R. Free-Atom-like d States in Single-Atom Alloy Catalysts. *Nature Chemistry* **2018**, 10 (10), 1008–1015. <https://doi.org/10.1038/s41557-018-0125-5>.
- (29) Tang, Y.; Asokan, C.; Xu, M.; Graham, G. W.; Pan, X.; Christopher, P.; Li, J.; Sautet, P. Rh Single Atoms on TiO₂ Dynamically Respond to Reaction Conditions by Adapting Their Site. *Nature Communications* **2019**, 10 (1). <https://doi.org/10.1038/s41467-019-12461-6>.
- (30) DeRita, L.; Resasco, J.; Dai, S.; Boubnov, A.; Thang, H. V.; Hoffman, A. S.; Ro, I.; Graham, G. W.; Bare, S. R.; Pacchioni, G.; Pan, X.; Christopher, P. Structural Evolution of Atomically Dispersed Pt Catalysts Dictates Reactivity. *Nature Materials* **2019**, 18 (7), 746–751. <https://doi.org/10.1038/s41563-019-0349-9>.
- (31) Larsen, J. H.; Chorkendorff, I. Increased Dissociation Probability of CH₄ on Co/Cu(111). *Surface Science* **1998**, 405 (1), 62–73. [https://doi.org/10.1016/S0039-6028\(98\)00045-4](https://doi.org/10.1016/S0039-6028(98)00045-4).
- (32) Sethuraman, V. A.; Vairavapandian, D.; Lafouresse, M. C.; Adit Maark, T.; Karan, N.; Sun, S.; Bertocci, U.; Peterson, A. A.; Stafford, G. R.; Guduru, P. R. Role of Elastic Strain on Electrocatalysis of Oxygen Reduction Reaction on Pt. *The Journal of Physical Chemistry C* **2015**, 119 (33), 19042–19052. <https://doi.org/10.1021/acs.jpcc.5b06096>.
- (33) Schlapka, A.; Lischka, M.; Groß, A.; Käsberger, U.; Jakob, P. Surface Strain versus Substrate Interaction in Heteroepitaxial Metal Layers: Pt on Ru(0001). *Physical Review Letters* **2003**, 91 (1), 016101/1-016101/4. <https://doi.org/10.1103/PhysRevLett.91.016101>.
- (34) Wang, S.; Petzold, V.; Tripkovic, V.; Kleis, J.; Howalt, J. G.; Skúlason, E.; Fernández, E. M.; Hvolbæk, B.; Jones, G.; Toftelund, A.; Falsig, H.; Björketun, M.; Studt, F.; Abild-Pedersen, F.; Rossmeisl, J.; Nørskov, J. K.; Bligaard, T. Universal Transition State Scaling Relations for (de)Hydrogenation over Transition Metals. *Physical Chemistry Chemical Physics* **2011**, 13 (46), 20760–20765. <https://doi.org/10.1039/c1cp20547a>.
- (35) Roling, L. T.; Abild-Pedersen, F. Structure-Sensitive Scaling Relations: Adsorption Energies from Surface Site Stability. *ChemCatChem* **2018**, 10 (7), 1643–1650. <https://doi.org/10.1002/cctc.201701841>.
- (36) Fields, M.; Tsai, C.; Chen, L. D.; Abild-Pedersen, F.; Nørskov, J. K.; Chan, K. Scaling Relations for Adsorption Energies on Doped Molybdenum Phosphide Surfaces. *ACS Catalysis* **2017**, 7 (4), 2528–2534. <https://doi.org/10.1021/acscatal.6b03403>.
- (37) Wittreich, G. R.; Liu, S.; Dauenhauer, P. J.; Vlachos, D. G. Catalytic Resonance of Ammonia Synthesis by Dynamic Ruthenium Crystal Strain. *ChemRxiv* **2021**, 1–12. <https://doi.org/10.33774/chemrxiv-2021-b8kgr>.
- (38) Wang, M.; Khan, M. A.; Mohsin, I.; Wicks, J.; Ip, A. H.; Sumon, K. Z.; Dinh, C. T.; Sargent, E. H.; Gates, I. D.; Kibria, M. G. Can Sustainable Ammonia Synthesis Pathways Compete with Fossil-Fuel Based Haber-Bosch Processes? *Energy and Environmental Science* **2021**, 14 (5), 2535–2548. <https://doi.org/10.1039/d0ee03808c>.
- (39) Che, F.; Ha, S.; McEwen, J. S. Elucidating the Field Influence on the Energetics of the Methane

- Steam Reforming Reaction: A Density Functional Theory Study. *Applied Catalysis B: Environmental* **2016**, 195, 77–89.
<https://doi.org/10.1016/j.apcatb.2016.04.026>.
- (40) Sutton, J. E.; Vlachos, D. G. A Theoretical and Computational Analysis of Linear Free Energy Relations for the Estimation of Activation Energies. *ACS Catalysis* **2012**, 2 (8), 1624–1634.
<https://doi.org/10.1021/cs3003269>.
- (41) Mhadeshwar, A. B.; Wang, H.; Vlachos, D. G. Thermodynamic Consistency in Microkinetic Development of Surface Reaction Mechanisms. *The Journal of Physical Chemistry B* **2003**, 107 (46), 12721–12733. <https://doi.org/10.1021/jp034954y>.
- (42) Campbell, C. T. The Degree of Rate Control: A Powerful Tool for Catalysis Research. *ACS Catalysis* **2017**, 7 (4), 2770–2779.
<https://doi.org/10.1021/acscatal.7b00115>.
- (43) Pearson, K. VII. Mathematical Contributions to the Theory of Evolution.—III. Regression, Heredity, and Panmixia. *Philosophical Transactions of the Royal Society of London. Series A, Containing Papers of a Mathematical or Physical Character* **1896**, 187, 253–318.
<https://doi.org/10.1098/rsta.1896.0007>.